Journal of Alloys and Compounds 863 (2021) 158341

Contents lists available at ScienceDirect

Journal of Alloys and Compounds

journal homepage: www.elsevier.com/locate/jalcom

An efficient vapor-phase processing method derived mesoporous N-C@SnO_2-Co_3O_4 hollow nanoboxes with abundant surface oxygen vacancy for highly improved gas sensing application

Minxuan Huang[a,b], Shaopeng Wang[a,b,c], Hao Fu[d], Hongyun Shao[a,b], Yinghui Wang[a,b,*], Kefu Yu[a,b,f], Yilin Huang[e], Zhiping Jv[e], Liwei Wang[a,b,c,f,*]

[a] School of Marine Sciences, Guangxi University, Nanning 530004, China
[b] Guangxi Laboratory on the Study of Coral Reefs in the South China Sea, Nanning 530003, China
[c] Guangxi Key Laboratory of Processing for Nonferrous Metals and Featured Materials, Nanning 530004, China
[d] School of Chemistry & Chemical Engineering, Guangxi University, Nanning 530004, China
[e] Radiation-Environment Management and Monitoring Station of Guangxi Zhuang Autonomous Region, 80 Rong Mo Road, Nanning 530222, China
[f] Southern Marine Science and Engineering Guangdong Laboratory (Zhuhai), Zhuhai 519080, China

ARTICLE INFO

Article history:
Received 31 October 2020
Received in revised form 13 December 2020
Accepted 13 December 2020
Available online 12 January 2021

Keywords:
Vapor-phase method
N-C dopant
Oxygen vacancy
SnO_2-Co_3O_4 hollow nanobox
Acetone selectivity

ABSTRACT

For widely used semiconductor-based chemoresistive sensors, low sensitivity and poor anti-interference in the complex environment (humidity resistance, *etc.*) are two main constraints of application. To enhance the sensitivity, many effective strategies have been developed such as constructing heterostructures with synergistic effects, introducing abundant oxygen vacancies as active sites, designing hollow/cavity structure to increase surface area to facilitate target gas adsorption, and so on. Besides, the interference caused by water vapor can be blocked.*via* MOF or molecular sieve membranes but is accompanied with the shielding of some target molecules. The above methods are faced with the problems of complex process, large workload of material screening and failure to maintain the device stability. Hence, an effective vapor-phase method derived N-C@SnO_2-Co_3O_4 complex that combined the hydrophobicity, acetone selectivity, p-n heterostructure with mesoporous hollow characteristics was proposed, named mesoporous N-C@SnO_2-Co_3O_4 hollow nanoboxes (HNBs). Particularly, the chemoresistive sensor based on N-C@SnO_2-Co_3O_4 HNBs (2.0%) showed satisfactory selectivity to acetone vapor at relatively low working temperature (160 °C), and the response remained stable even under high humidity (with the R.H. of 90%). Impressively, a three-fold enhancement in response signal was observed for the sensor based on N-C@SnO_2-Co_3O_4 HNBs when compared with its counterpart of SnO_2-Co_3O_4, which can be ascribed to the consequent unpaired electrons from oxygen vacancies and hollow mesoporous structures. Additionally, a sensing prototype based on the N-C@SnO_2-Co_3O_4 HNBs was practically fabricated. The satisfactory sensing response and stability further verified the potential applications in industrial acetone detection. This facile vapor-phase approach sheds light on designing sensing materials with enhanced sensitivity and humidity resistance, as well as device stability simultaneously.

1. Introduction

In recent years, metal oxide semiconductor (MOSs) gas sensors have attracted tremendous attention due to their extraordinary properties and have been successfully applied in detection of toxic or explosive gases in war industries, in-house measurements of dangerous gases and air quality, alongside emerging applications in medical diagnostics and food/cosmetic quality control [1–3]. However, their working performances are still deviated from ideal demand, and faced with the technical issues especially as low sensitivity and decreased stability under external interference gas disturbances [4].

To solve the problem of low sensitivity, there are two strategies. Heterostructures can be constructed to improve sensitivity by a synergistic effect [5,6]. Oxygen defects, as the active sites, can also be introduced by hydrogen treatment, solid phase reduction, flame

* Corresponding authors at: School of Marine Sciences, Guangxi University, Nanning 530004, China
E-mail addresses: wyh@gxu.edu.cn (Y. Wang), wangliwei0427@163.com (L. Wang).

https://doi.org/10.1016/j.jallcom.2020.158341
0925-8388/

reduction method and other methods [7–9], which play a critical role to enhance the gas sensing efficiency as they not only promote oxygen adsorption, but also facilitate the charge transportation and the formation of surface catalytic active species to improve the degree of a surface redox reaction [10,11]. Furthermore, the filter strategies derived from the molecular sieves or MOF caps do eliminate some negative interference effectively, but the response signal is inevitably reduced by screening some target gas molecules, which is definitely unfavorable to make full use of the exposed active catalytic sites [12–14]. Besides, it also can try to design the core-shell structure and use the hydrophobicity of the shell to improve the humidity resistance of the device, etc [15]. However, these works put forward high requirements for the screening of gas sensing materials, and there are few materials with these excellent properties. Therefore, it's of great significance to construct a novel MOSs material that can both improve gas selectivity effectively even under the negative impact (*e.g.* high humidity), and maintain the desirable response.

Based on this, we propose an efficient method to integrate all the above characteristics into one material, namely one-step construction of N-C@SnO_2-Co_3O_4 hollow nanoboxes (HNBs) by vapor-phase processing method. This method is to introduce oxygen vacancy into organic-inorganic hollow heterostructure, and the addition of organic cladding layer can enhance the adsorption of specific gases, play a shielding role on water molecules, and improve the selectivity of the device, even in a high humidity atmosphere. Hence, the sensor of N-C@SnO_2-Co_3O_4 HNBs exhibits a sufficient acetone adsorption preferred reaction, and it can also block the interference from other surrounding gases or water vapor, so as to enhance humidity resistance (R.H.: 5–90%), selectivity and sensitivity. Besides, a sensing prototype is built and operated in real working conditions, which further conform our work provides a significant strategy for acetone gas sensor selective sensing arrays application at a high humidity atmosphere.

2. Experimental section

2.1. Materials and synthesis

All the chemical reagents in the experiment were of analytical reagent and used as received without further purification. Stannic chloride hydrated ($SnCl_4{\cdot}5H_2O$), cobalt chloride hexahydrate ($CoCl_2{\cdot}6H_2O$), sodium citrate tribasic dihydrate ($C_6H_5Na_3O_7{\cdot}2H_2O$) and sodium hydroxide (NaOH) were purchased from Aladdin Industrial Corporation (Shanghai, China). Anhydrous alcohol (CH_3CH_2OH) was purchased from Sinopharm Chemical Reagent Co. Ltd. (Shanghai, China). Deionized water was used in the synthesis procedures.

The synthesis strategies of N-C@SnO_2-Co_3O_4 hollow nanoboxes (HNBs) and SnO_2-Co_3O_4 HNBs were schematically illustrated in Fig. S1. The $CoSn(OH)_6$ HNB precursor was synthesized by the co-precipitation method with some modification from the previous work, as had been described in supporting information [16]. Then, N-C@SnO_2-Co_3O_4 HNBs were synthesized *via* a vapor-phase processing method. First, a certain amount of $CoSn(OH)_6$ precursor was put onto the bottom of a smaller crucible, which was placed upside down in a larger crucible, as shown in Fig. S1. While 75 mg of 2-Methylimidazole was evenly sprinkled to the bottom of the larger crucible. And then, the entire combination was wrapped with three layers of tin foil. Afterward, the whole container was annealed in a muffle furnace at 450 °C for 2 h in air, and finally the brown product was collected for further use, which was denoted as N-C@SnO_2-Co_3O_4 HNBs (2.0%) after the thermal gravimetric analysis. For reasonable comparison of sensor performance, the sample without N-C doping was also treated in the same way as the N-C doped one but in the absence of 2-Methylimidazole, and the treated sample is named as annealed SnO_2-Co_3O_4 HNBs to be distinct from the as-synthesized sample. Besides, to discuss the role and impact of N-C dopant and oxygen vacancy on the gas sensing performance, 50 and 100 mg of 2-Methylimidazole to respectively anneal with $CoSn(OH)_6$ as the same way, which were denoted as N-C@SnO_2-Co_3O_4 HNBs (0.9%) and N-C@SnO_2-Co_3O_4 HNBs (2.5%) after the thermal gravimetric analyses.

2.2. Materials characterization

The samples were characterized by means of powder XRD analysis (Rigaku Ultima IV, Japan, Cu Kα radiation, λ = 1.5418 Å), Field-emission SEM (Hitachi SU5000, Japan), TEM and HRTEM with EDS (FEI TeN-Cai G2 f20 s-twin, 200 kV), XPS (Thermo SCIENTIFIC ESCALAB 250Xi, Al Kα X-ray monochromator), BET (Autosorb-IQ, USA), Raman spectroscopy (Renishaw inVia, UK), Steady state and transient state fluorescence spectrometer (HORIBA TCSPC FluoroLog-3, USA), TG-FTIR (TGA 8000-FT-IR, PerkinElmer, USA), UV/Vis (PE 950, PerkinElmer, USA), Electron spin resonance (JES-FA300, Japan).

2.3. Sensor fabrication and gas-sensing test

The preparation and measurement of the side-heating sensor were similar to those depicted in our previous report [17]. Firstly, the prepared sample and deionized water were mixed together in an agate mortar to make a paste by grinding. The paste was then coated evenly to the surface of the ceramic tube, which was welded with Ni-Cr heater onto the pedestal and inserted into the test channel. Gas-sensing tests were carried out through the CGS-8 intelligent test system (Beijing Elite Tech Co. Ltd., China). Especially, to investigate the influence of relative humidity (R.H.) on the gas sensing performance, we pre-mixed the water vapor with acetone vapor and air at room temperature of 25 °C by the DGL-III humidity control gas and liquid distribution system to reach specific relative humidity. Afterwards, the mixed gases were put into the test chamber of the CGS-8 intelligent test system. This intelligent test system adopts automatic control and intelligent software management, which can provide precise control of gas flow, dilution, relative humidity, *etc.* Hence, the relative humidity was instrumentally controlled by the dynamic gas distribution system, while the accuracy would be ensured. The sensor response (S) was defined as the ratio of R_g/R_a, where R_a and R_g were the resistances measured in air and the tested gas atmosphere, respectively [18,19].

3. Results and discussion

For the purpose of simultaneously tailoring the level of oxygen vacancy and enhancing the capability of humidity resistance, a simple and effective vapor-phase strategy is proposed and adopted to synthesize metal oxide for gas sensing (Supplimentary Fig. 1). It is spatulated that the vapor-phase treatment would significantly increase the the level of oxygen vacancy, whilst, a N-C shell will additionally form on the surface of sensing material, mitigating negative impact derived from high humidity. Note that, in this study SnO_2-Co_3O_4 nanocomposite is selected as the example and chemical modified to demonstrate the possibility of relatizing the expected research objective through the proposed strategy.

Initially, microstructure of the wet route resulted SnO_2-Co_3O_4 HNBs and vapor-phase obtained N-C@SnO_2-Co_3O_4 HNBs (2.0%) was characteristics and compared. Fig. 1 gives the the X-ray diffraction (XRD) patterns for the crystal structures of SnO_2-Co_3O_4 HNBs and N-C@SnO_2-Co_3O_4 HNBs. Both samples are composed of two types of diffraction peaks, which can be assigned to rutile SnO_2 (JCPDS: 41–1445) and cubic Co_3O_4 (JCPDS: 42–1467). Note that the diffraction peaks of N-C@SnO_2-Co_3O_4 HNBs (2.0%) are significantly broadened in width and weaken in intensity. According to the Scherrer equation, the crystallite sizes of SnO_2-Co_3O_4 HNBs and N-C@SnO_2-

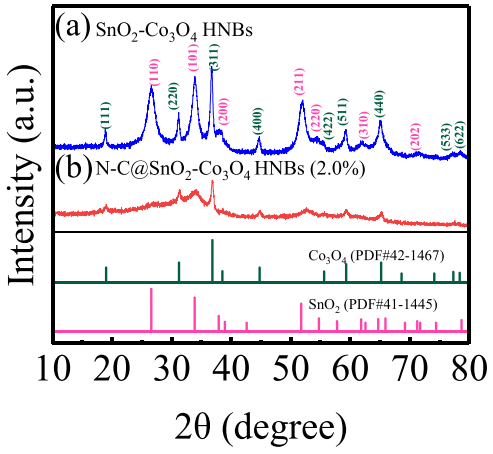

Fig. 1. XRD patterns of (a) SnO_2-Co_3O_4 HNBs and (b) N-C@SnO_2-Co_3O_4 HNBs (2.0%).

Co_3O_4 HNBs (2.0%) are evaluated based on the diffraction peak of (101), and the values are from 8 down to 4 nm respectively. This suggests the nanosized crystal structure is well readjusted in N-C@ SnO_2-Co_3O_4 HNBs (2.0%) during the vapor-phase processing method. In addition, it is well known that the grain size approaches to Debye length (λ_D, usually several nm), the increase of sensitivity is more obvious due to the effect of grain size [20]. At the same time, the decrease of grain size also increases the specific surface area to increase the active site of N-C@SnO_2-Co_3O_4 HNBs (2.0%) [21]. Therefore, changing the physical properties of the N-C@SnO_2-Co_3O_4 HNBs (2.0%) by doping with the N-C shows an effective approach to increasing sensitivity. Furthermore, the evidence and insight of comprehensive characterizations should be required to explain the enhancement of gas sensing performance, such as, Raman spectroscopy, Fourier Transform infrared spectroscopy (FTIR), Photoluminescence (PL) spectroscopy, electron spin resonance (ESR) measurement, and so on.

SEM images of SnO_2-Co_3O_4 HNBs and N-C@SnO_2-Co_3O_4 HNBs (2.0%) are provided in Fig. 2a and b, and both of the samples display hollow box-like structures with an average edge length of 600 nm. Compare with these two figures, nanoparticles with a diameter of about 15 nm appeared on the surface of N-C@SnO_2-Co_3O_4 HNBs (2.0%). This may be due to the coordination of Co^{2+} in 2-Methylimidazole and $CoSn(OH)_6$, which results in the different precipitation rate of Co_3O_4 coordinated by 2-Methylimidazole during the heterogeneous thermal decomposition of $CoSn(OH)_6$ compared with that before without 2-Methylimidazole treatment, resulting in recrystallization, which can be confirmed by the analysis of EDS (Fig. S2). In Fig. 2c, HRTEM image displays clear lattice fringes of 2.85 and 2.37 Å, matching well with the (220) lattice plane of Co_3O_4 and the (200) lattice plane of SnO_2, respectively. This proves the heterophase of the calcined N-C@SnO_2-Co_3O_4 HNBs (2.0%). Moreover, the porosity of the material is one of the important factors affecting gas diffusion, which is essential in the gas sensing performance. TEM of Fig. 2d shows that highly dense nanopores are distributed onto the N-C@SnO_2-Co_3O_4 HNBs (2.0%) surface. The N_2 adsorption-desorption isotherm is further carried out on N-C@SnO_2-Co_3O_4 HNBs (2.0%) in Fig. S3, and the result shows that the specific surface area is 66.15 m^2/g. Additionally, the inner illustration in Fig. S3 indicated the appearance of one sharp peak centered at about 5.62 nm. It indicates the comparatively uniform mesoporous size of N-C@SnO_2-Co_3O_4 HNBs (2.0%). Such a regular mesoporous structure of sensor with pore channels in the range of 4–6 nm serves to increase the adsorption/desorption rate of target gas or water molecules and deliberately increases the charge carrier transmission across the sensor surface [22]. In addition, constructing a hollow structure with a mesoporous surface can efficiently expose the active sites of N-C catalysts to provide the easy accessibility of O_2 and electrolytes [23]. To explore the doping amount of N-C, the thermal gravimetric analysis (TG) analysis of SnO_2-Co_3O_4 HNBs and N-C@SnO_2-Co_3O_4 HNBs (2.0%) are presented in Fig. S4a, where a slight mass redu–c-tion occurs up to about 670 °C. This finding directly evidences that the dissociation of N-C with the doping amount is about 2.0%. Besides, to prove the existence of N and C elements, the detailed thermal decomposition process has been dynamically explored by TG-FTIR combination analysis, as shown in Supplimentary Fig. S4b and c. As can be seen in Supplimentary Fig. S4b, the heating temperature is from 30 to 750 °C under N_2 gas. Notably, two distinct FTIR peaks are detected as peak A and B. The peak A at 118 °C is indexed to the desorption of physical-adsorbed H_2O, CO_2 molecules and the organic impurities, while peak B at about 658 °C suggested the obvious phase formation due to the decomposition of N-C@SnO_2-Co_3O_4 HNBs (2.0%) [24]. In Fig. S4c, the *in-situ* FTIR spectrum of N-C@SnO_2-Co_3O_4 HNBs (2.0%) is performed to prove the existence of N element and related bonds, corresponding to the thermal decomposition temperature at 658 °C, where the absorption peaks at 3000–3600, 2370, 1650 and 1540 cm^{-1} can be ascribed to stretching vibrations of N-H, O=C=O, C≡N and C–N, respectively [25–30]. Without a doubt, it is confirmed that N and C elements could be successfully doped on the surface of N-C@SnO_2-Co_3O_4 HNBs (2.0%) product.

X-ray photoelectron spectroscopy (XPS) is used to clarify the valence chemistry and binding energy of the elements in SnO_2-Co_3O_4 HNBs and N-C@SnO_2-Co_3O_4 HNBs (2.0%). Except for the peaks of Sn, Co and O, very trace N and C elements can be seen in the XPS spectra of N-C@SnO_2-Co_3O_4 HNBs (2.0%) (Figs. 3a and S5), which is corresponding to the result from the TG analysis in Fig. S4, suggesting that the surface of N-C@SnO_2-Co_3O_4 HNBs (2.0%) is successfully modified *via* the vapor-phase processing method. Furthermore, the O 1 s peak for each composite can be fitted into three Gaussian simulation peaks in Fig. 3b. The datum confirms the existence of three different chemical states of oxygen species: lattice oxygen (O_L) belonging to the Co-O bonds and Sn-O bonds, oxygen vacancy (O_V) and chemisorbed oxygen (O_C) [31–33]. Table 1 summarizes the relative percentage of oxygen chemical states on the surface of SnO_2-Co_3O_4 HNBs and N-C@SnO_2-Co_3O_4 HNBs (2.0%) respectively. Notably, comparing with SnO_2-Co_3O_4 HNBs, the contents of O_V and O_C in N-C@SnO_2-Co_3O_4 HNBs (2.0%) are greatly increased. It proves that the gas sensing properties are closely related to the O_V and O_C in N-C@SnO_2-Co_3O_4 HNBs (2.0%). In addition, it is speculated that the increase of O_C is the result of the increase of O_V, since the O_V could provide active sites for the oxygen adsorption and reaction on the surface of the sensing materials. So the increase in O_V content means that more O_C species could participate in the oxidation-reduction reaction occurring on the surface of the sensing materials and thus cause a larger enhancement in sensor response [20]. Moreover, the X-ray absorption fine structure (XAFS) is used to examine the local atom structural environment, which can be carried out to further analyze the oxygen species because of the element-specific techniques [34,35]. And this problem has been recognized and will be researched in this area, which will be the next focus of our work.

As indicated above, it can be inferred more oxygen vacancy defects lie in the N-C@SnO_2-Co_3O_4 HNBs (2.0%), furthermore, Raman spectroscopy and PL measurement are carried out to assist the further confirmation. In Fig. 4a, the Raman spectra of SnO_2-Co_3O_4 HNBs and N-C@SnO_2-Co_3O_4 HNBs (2.0%) in the range of wavenumber 150–950 cm^{-1} are recorded at room temperature. Typically, the peaks contain at about 512.4 and 670.8 cm^{-1} are assigned as SnO_2 and Co_3O_4, which verify the accuracy of XRD spectra [36,37]. Moreover, the peaks at about 593.0 cm^{-1} detected in the two samples are ascribed to the surface oxygen vacancies, in which the obtaining peaks match with previously reported [38]. To investigate the category and quantity of the defects, the ESR measurements of

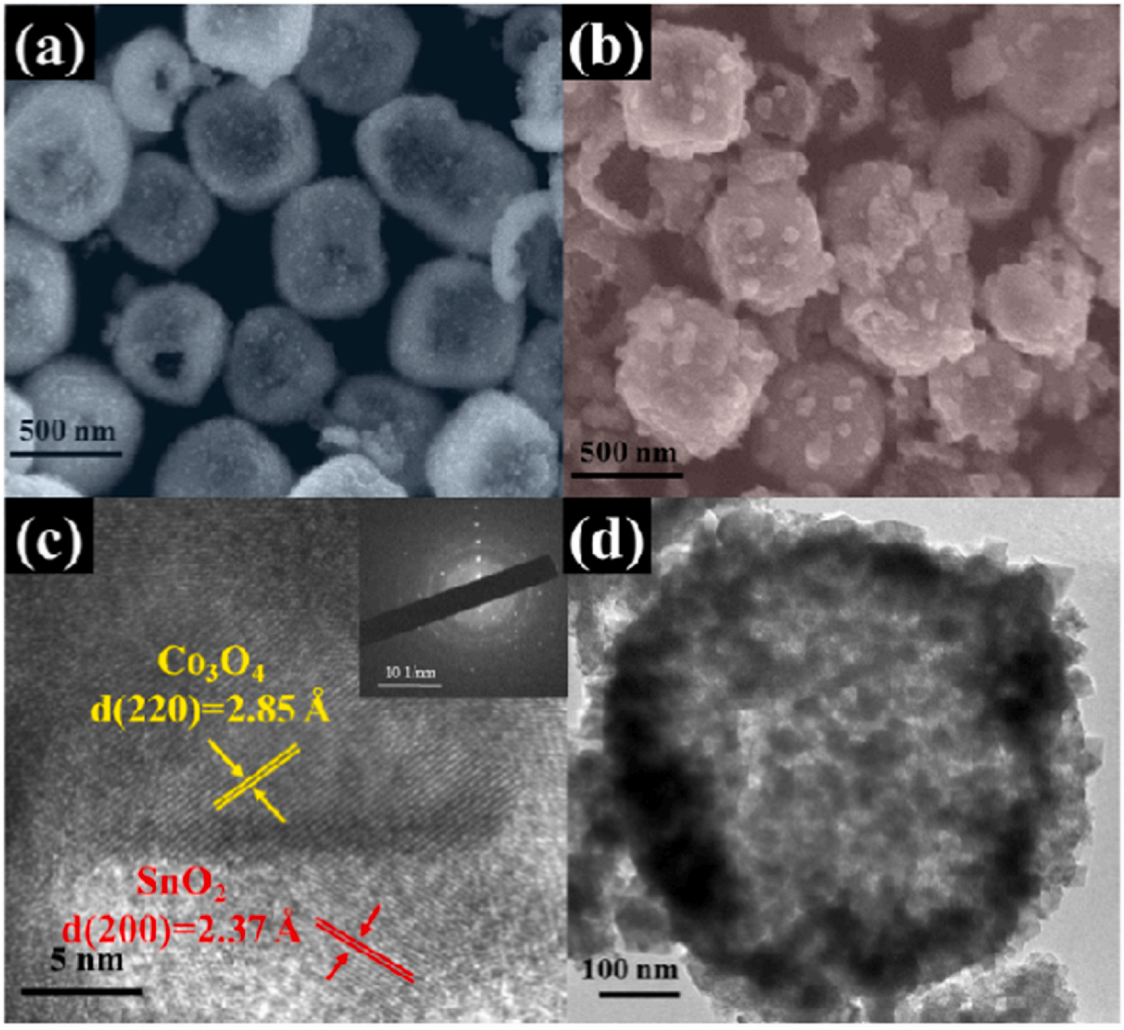

Fig. 2. (a, b) SEM images of SnO_2-Co_3O_4 HNBs and N-C@SnO_2-Co_3O_4 HNBs (2.0%), (c) HRTEM image and (d) TEM image of N-C@SnO_2-Co_3O_4 HNBs (2.0%).

SnO_2-Co_3O_4 HNBs and N-C@SnO_2-Co_3O_4 HNBs (2.0%) are obtained in Fig. 4c, where a broad peak at g = 1.99 is identified and corresponded to the electrons trapped in oxygen vacancies [39]. The intensity of the peak is higher for N-C@SnO_2-Co_3O_4 HNBs (2.0%) than for SnO_2-Co_3O_4 HNBs, demonstrating the successful introduction of oxygen vacancies into N-C@SnO_2-Co_3O_4 HNBs (2.0%). This result is consistent with the results of XPS, PL and Raman spectroscopies. Besides, Fig. 4d illustrates the electronic band structures of both SnO_2-Co_3O_4 HNBs and N-C@SnO_2-Co_3O_4 HNBs (2.0%). It has been shown an obviously narrowed bandgap (E_g) from 3.2 eV down to 3.0 eV, which is consistent with the report that oxygen vacancies as electron donors can lead to bandgap narrowing by tuning the electronic structure of MOS [40]. Although oxygen vacancies do not lead to a large decrease in the bandgap, the energy barrier required for species to move through the space charge region can be modified, making room temperature applications more of a reality by changing the bandgap values [41]. This can have even wider implications that fine-tuning materials will be better for specific applications (*e.g.* the narrowed bandgap is beneficial for the transfer of thermal-induced electrons to affect the optimum working temperature, selectivity or

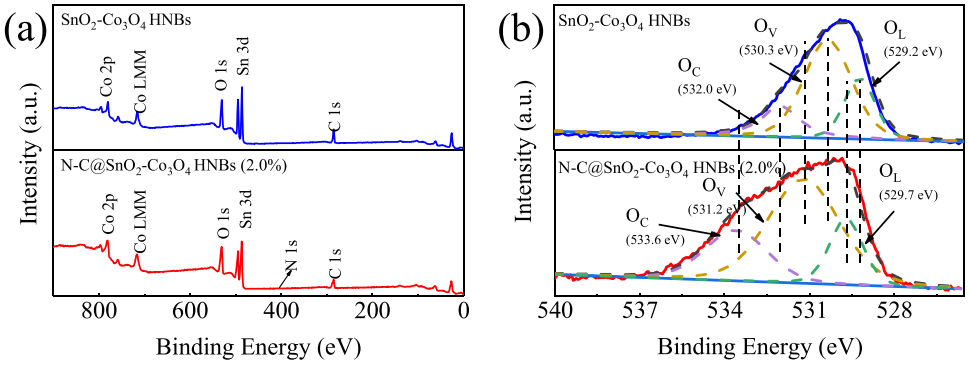

Fig. 3. XPS spectra of the (a) survey and (b) high magnification of O 1 s based on SnO_2-Co_3O_4 HNBs and N-C@SnO_2-Co_3O_4 HNBs (2.0%).

Table 1
Results of curve fitting of O 1 s XPS spectra of SnO_2-Co_3O_4 HNBs and N-C@SnO_2-Co_3O_4 HNBs (2.0%).

Sample	O_L		O_V		O_C	
	Binding energy (eV)	Relative percentage (%)	Binding energy (eV)	Relative percentage (%)	Binding energy (eV)	Relative percentage (%)
SnO_2-Co_3O_4 HNBs	529.5	40.63	530.7	52.13	532.5	7.24
N-C@SnO_2-Co_3O_4 HNBs (2.0%)	529.7	20.21	531.2	55.31	533.6	24.48

response/recovery speeds of the sensor) [42]. Thus, all the characterization analyses verified the sensing results of Fig. 5 that the N-C@SnO_2-Co_3O_4 HNBs (2.0%) sensor with more oxygen adsorption and higher electron mobility could be contributed to the surface reaction between the adsorbed oxygen and test gas, which is good for the improvement of gas sensing performance.

To confirm the assumption, gas sensors based on SnO_2-Co_3O_4 HNBs and N-C@SnO_2-Co_3O_4 HNBs (2.0%) are fabricated and their gas-sensing performances have been investigated. Besides, other amounts of N-C doping samples, such as N-C@SnO_2-Co_3O_4 HNBs (0.9%) and N-C@SnO_2-Co_3O_4 HNBs (2.5%), are prepared to compare with SnO_2-Co_3O_4 HNBs and N-C@SnO_2-Co_3O_4 HNBs (2.0%) in Figs. S8 and S9. Fig. S8 presents the response of four sensors at different operating temperatures from 140 to 180 °C. These four sensors show the same tendency of "increase-maximum-decay" in the entire range, and their optimum working temperatures are 160 °C. Besides, combined with the result of Fig. S9, it can be deduced that the loading amount of the N-C dopant affects the amount of oxygen vacancies and has a great influence on response performance in the whole sensing test. With the highest oxygen vacancies concentration, N-C@SnO_2-Co_3O_4 HNBs (2.0%) is found to be most optimal for gas sensing application with regard to response and selectivity toward acetone vapor sensing tests. But when the excess amount of N-C loading, it may occupy aggregation and fewer oxygen vacancies of SnO_2-Co_3O_4, which will hinder the surface sensing reaction and decrease the MOS sensor response.

Humidity for the sensor is another concerning issue in real applications. To quantify the effect of humidity on the chemiresistive sensing behaviors of the samples, we calculated the ratios of the sensor resistances (Ra_{-wet}/Ra_{-dry}) at 160 °C in dry air and 90% R.H. in Fig. 5a-i and a-ii [43,44]. Sensors with $Ra_{-wet}/Ra_{-dry} \geq 1$ show the humidity-independent gas response and sensor resistance in air, respectively. The Ra_{-wet}/Ra_{-dry} values lower than 1 indicate a large decrease in the gas response and sensor resistance by moisture, respectively. Note that for the N-C@SnO_2-Co_3O_4 HNBs (2.0%) sensor, the Ra_{-wet}/Ra_{-dry} values tended to move closer to unify with increasing R.H. values from 30% to 90%, indicating that the chemiresistive type sensors maintained the humidity resistance property. Besides, in Fig. 5b, the gas selectivity of the SnO_2-Co_3O_4 HNBs and N-C@SnO_2-Co_3O_4 HNBs (2.0%) sensors under dry or humid (90% R.H.) atmospheres are measured at 160 °C, while the gas responses under the dry and humid conditions are similar, namely excellent selectivity response to acetone under both dry and humid atmospheres. Particularly, Fig. S10 has shown the actual change in Rg values of the N-C@SnO_2-Co_3O_4 HNBs (2.0%) sensor to 50 ppm of acetone under different levels of R.H. at 160 °C. And the sensing profiles of the N-C@SnO_2-Co_3O_4 HNBs (2.0%) sensor at 160 °C are shown in Fig. 5c. It can be found that the response of the N-C@SnO_2-

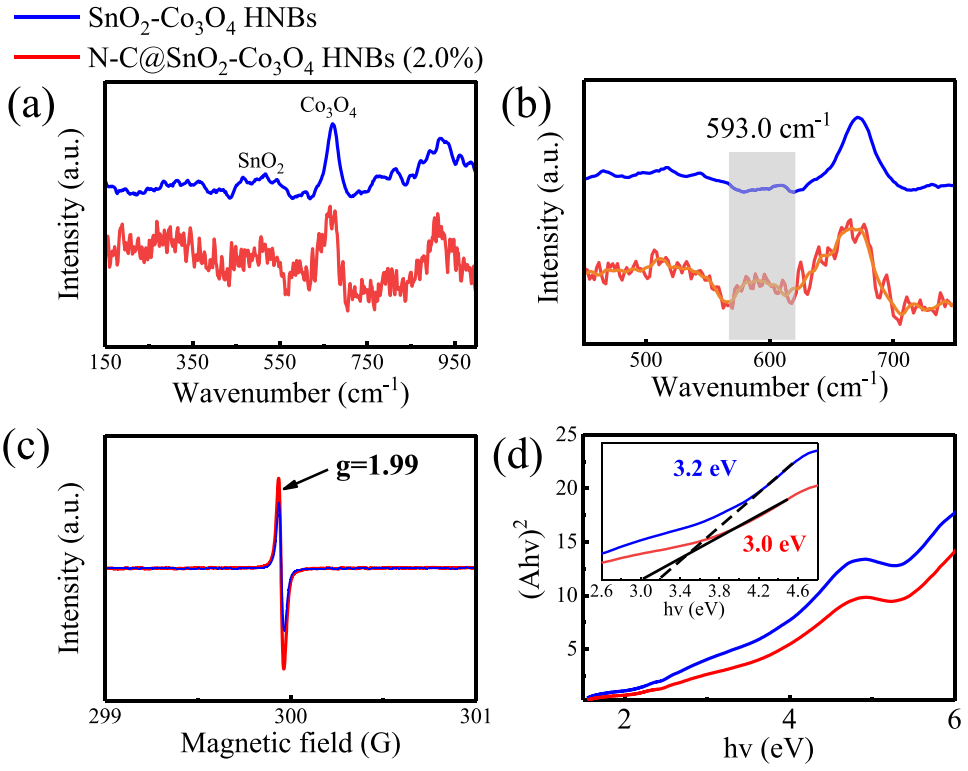

Fig. 4. (a) Raman spectra, (b) zoomed Raman spectra between 450 and 750 cm^{-1}, (c) ESR spectra and (d) optical bandgaps determined by UV-Vis diffuse reflectance spectra of SnO_2-Co_3O_4 HNBs and N-C@SnO_2-Co_3O_4 HNBs (2.0%).

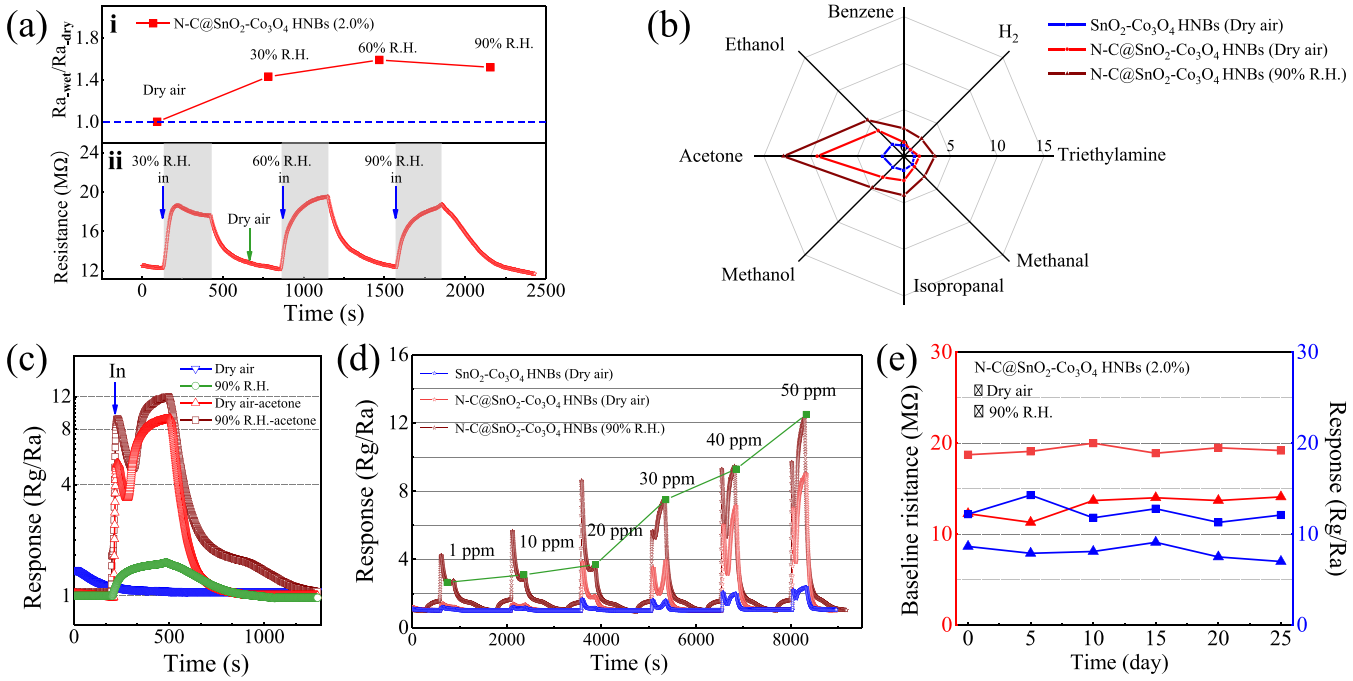

Fig. 5. (a)-i: The Ra_{-wet}/Ra_{-dry} values and (a)-ii: resistances of N-C@SnO_2-Co_3O_4 HNBs (2.0%) at 160 °C in different relative humidity (dry air, 30%, 60% and 90% R.H.), (b) Selectivity of SnO_2-Co_3O_4 HNBs and N-C@SnO_2-Co_3O_4 HNBs (2.0%) to 50 ppm of different gases at 160 °C in dry air or 90% R.H., (c) Dynamic response of N-C@SnO_2-Co_3O_4 HNBs (2.0%) at 160 °C in different atmospheres (dry air, 90% R.H., dry air-50 ppm acetone and 90% R.H.–50 ppm acetone), (d) Dynamic sensing transients of SnO_2-Co_3O_4 HNBs and N-C@SnO_2-Co_3O_4 HNBs (2.0%) upon the exposure to 1–50 ppm of acetone at 160 °C in dry or 90% R.H., (e) Baseline resistances and responses of N-C@SnO_2-Co_3O_4 HNBs (2.0%) to 50 ppm acetone at 160 °C in dry air and 90% R.H.

Co_3O_4 HNBs (2.0%) tends to be stable in dry air without injecting acetone, while the response increased to 9 rapidly after acetone injection. Even in 90% R.H., the corresponding response is no more than 2, but the response increased to 12 after acetone injection in such high humidity. The common character of the sensors is the adsorption of water on their surfaces, indicating the positive effect of water on the acetone sensing reactions. Thus, these results clearly indicate that the N-C@SnO_2-Co_3O_4 HNBs (2.0%) sensor can be implemented for the practical acetone analysis regardless of the humidity variation.

The most interesting point observed from Fig. 5 and Figs. S10–12 is that the sensor resistance rises slightly during the pre-injection of the humid vapor, and this 'signal drift' phenomenon is caused by the 'donor effect' [45,46]. The 'donor effect' has been attributed to that water molecules replace the previously adsorbed and ionized oxygen (O^-, O^{2-}, *etc.*) on the surface of MOS, therefore, release the electrons from the ionized oxygen. This process releases the electrons back to N-C@SnO_2-Co_3O_4 HNBs (2.0%), which narrows the accumulation layer of holes by electron-hole recombination, leading to an increase of resistance [47–50]. Thus, this is probably because of the abundant surface oxygen vacancy defects and large specific surface area of N-C@SnO_2-Co_3O_4 HNBs (2.0%), which play an essential role in boosting the humidity sensing performance. The surface oxygen vacancy defects could provide a high local charge density and a strong electrostatic field *via* a dissociative chemisorption process [51]. The enhanced water dissociation triggered by surface oxygen vacancy defects is beneficial for hopping transportation of protons on the surface, which is demonstrated to be the dominant conduction process in the humidity sensing test. Besides, the abundant adsorption sites provided by the large specific surface area of mesoporous N-C@SnO_2-Co_3O_4 HNBs (2.0%) also expedite the electrolytic conduction process, resulting in further enhanced response at high R.H. level [51].

Moreover, all sensors can effectively detect acetone gas under various concentrations (1–50 ppm). With the increasing acetone concentration, the response of N-C@SnO_2-Co_3O_4 HNBs (2.0%) sensor increases in magnitude from 2.5 at 1 ppm to 12.1 at 50 ppm and exhibits the highest response compared to another sensor in 90% R.H. as shown in Fig. 5d. Furthermore, repeatability is also an important parameter to evaluate the reliability of the sensor for real-life applications. The sensors demonstrate good reversibility, maintaining stable baselines and rapid response during consecutive 1 or 50 ppm acetone cycles in dry air or even in 90% R.H., as shown in Fig. S9b, c and S12. In addition, no obvious decrease in the baseline resistance and response are observed in the N-C@SnO_2-Co_3O_4 HNBs (2.0%) sensor over 25 days, even in 90% R.H., confirming the highest long-term stability of N-C@SnO_2-Co_3O_4 HNBs (2.0%) (Fig. 5e).

At last, Table 2 lists a comparison of the key performance parameters of the N-C@SnO_2-Co_3O_4 HNBs (2.0%) sensor with some typical MOSs sensors, such as the working temperature, cites the effect of oxygen vacancies and humidity effect. In most studies, the ideal amount of dopant is often cited as being one that optimizes the number of oxygen vacancies, producing the highest response, being reported. As can be seen, the N-C@SnO_2-Co_3O_4 HNBs (2.0%) synthesized through N-C doping for detecting acetone is superior to other sensors in 90% R.H. previously reported, regarding humidity resistance, stability and working temperature. Besides, a portable sensing prototype with excellent gas sensing performance is assembled for remote monitoring of acetone *via* wireless transmission, which has been depicted in our previous work [56]. As shown in Fig. S13, a real-time response signal in terms of resistance changes are transmitted *via* bluetooth and appeared in the application interface. Thus, the success of our proposed strategy offers an efficient and convenient approach to modify the sensing properties of the sensor towards the expected research objective.

The gas-sensing mechanism of the N-C@SnO_2-Co_3O_4 HNBs (2.0%) involves the surface-related redox reaction which can be explained by the surface depletion layer model reported in previous kinds of literature [9,57,58]. It mainly depends on the change of electrical conductivity caused by the interaction between the tested gases and

Table 2
Comparison of different sensors report in kinds of literature.

Material	Target gas	Working temp (°C)	Concn (ppm)	Response (dry air/high R.H.)	Cited effect of O_V	Res. *vs* R.H.	Refs.
rGO-Co_3O_4 composites	NO_2	100	5	30/11	Increased O_C from increased O_V	Negative	[52]
Pt-In_2O_3 nanofibers	Acetone	180	1	15/9	Increased O_V from doping Pt	Negative	[24]
Au-SnO_2 nanotubes	Acetone	200	50	20/7	Increased O_C	Negative	[53]
Co-SnO_2 nanofibers	Ethanol	300	50	20/-	Increased O_C from increased O_V	-	[54]
Pt-decorated Al-doped ZnO nanoparticles	Acetone	450	10	421/50	Increased O_V from doping Pt and Al	Negative	[55]
N-C@SnO_2-Co_3O_4 HNBs (2.0%)	Acetone	160	50	9.25/14	Increased O_V from doping N-C	Humidity resistant	This work

the ionized oxygen species (mainly O^- at 160 °C in our work) onto the material surface [59]. The sensing mechanisms of N-C@SnO_2-Co_3O_4 HNBs (2.0%) in air and target gas are schematically shown in Fig. 6a and b. In general, when the N-C@SnO_2-Co_3O_4 HNBs (2.0%) based sensor is exposed to an air atmosphere, the oxygen molecules can be adsorbed on the surface of the N-C@SnO_2-Co_3O_4 HNBs (2.0%) and capture free electrons from the conduction band of the material. Then the adsorbed oxygen will form the chemisorbed oxygen species O^-, which turns to a hole depletion layer on the surface and forms the potential barrier. When a sensor based on N-C@SnO_2-Co_3O_4 HNBs (2.0%) is exposed to acetone vapors, the acetone molecules will react with the adsorbed oxygen and release the electrons trapped from the material conduction band back. This reaction increases the electron concentration of the composite, that is, more electrons flow to neutralize the holes, resulting in the thickening of the depletion layer, the increase of resistance, and the improvement of response.

The enhancement in acetone-response property of the sensor based on N-C@SnO_2-Co_3O_4 HNBs (2.0%) can be explained as follows. Firstly, the appropriate amount of N-C doping could enhance the acetone sensing properties by inducing surface oxygen vacancies in the synthesized material. Based on all defect characterization results, more oxygen vacancies observed in N-C@SnO_2-Co_3O_4 HNBs (2.0%). As electron donors, oxygen vacancies provide unpaired electrons for oxygen adsorption and ionization, suggesting more active chemisorbed-oxygen-sites to react with acetone in N-C@SnO_2-Co_3O_4 HNBs (2.0%) than SnO_2-Co_3O_4 HNBs [40]. Moreover, oxygen vacancies on the surface are reported to dissociate water through the transfer of one proton to a nearby oxygen atom, enhancing the chemisorption of the dissociative water molecules, which provides a high local charge density and a strong electrostatic field *via* a dissociative chemisorption process. To analyze the adsorption of acetone, the FTIR analysis of N-C@SnO_2-Co_3O_4 HNBs (2.0%) pre-treated by saturation adsorption of acetone are tested in Fig. S14. Before the FTIR test, the N-C@SnO_2-Co_3O_4 HNBs (2.0%) based sensor was pre-treated by saturation adsorption of acetone. As can be seen, the wavenumber from 1514 to 1637 cm^{-1} can be ascribed to the existence of N-H and C-N stretching vibrations. These results suggest that the partial reaction of acetone still maintained a good form of chemi-adsorption on the surface of N-C@SnO_2-Co_3O_4 HNBs (2.0%) at 100 °C because of highly polar nature of acetone and low dissociation energy of CH_3-$COCH_3$ bond, accompanied by a small amount of oxidation [43]. Therefore, an abundance of surface oxygen vacancies on the surface is expected to enhance selectivity and response, regardless of humidity change. Secondly, oxygen vacancies narrow the bandgap of N-C@SnO_2-Co_3O_4 HNBs (2.0%) from 3.2 eV down to 3.0 eV, which improves the transition of electrons and the adsorption or activation of the target gas. Lastly, the prepared material is a hollow structure with uniform mesoporous (Pore Diameter: 5.62 nm). Such a structure is favorable for acetone diffusion and improves the kinetics of the reaction of the acetone molecules with oxygen species. And the abundant adsorption sites provided by the large specific surface area of mesoporous N-C@SnO_2-Co_3O_4 HNBs (2.0%) could expedite the electrolytic conduction process, resulting in an enhanced response at high R.H. level. To sum up, the factors synergistically contribute to improving gas sensing performance. Moreover, the exact mechanism for the improved acetone selectivity through the addition of N-C@SnO_2-Co_3O_4 HNBs (2.0%) still needs further studies.

4. Conclusion

Aiming to efficiently tuning the abundant surface oxygen vacancy defects that can help obviously enhance gas selectivity and the response of the semiconductor heterostructure-based chemical sensor, we designed mesoporous N-C@SnO_2-Co_3O_4 hollow nanoboxes (HNBs) *via* a unique vapor-phase processing method. And compared

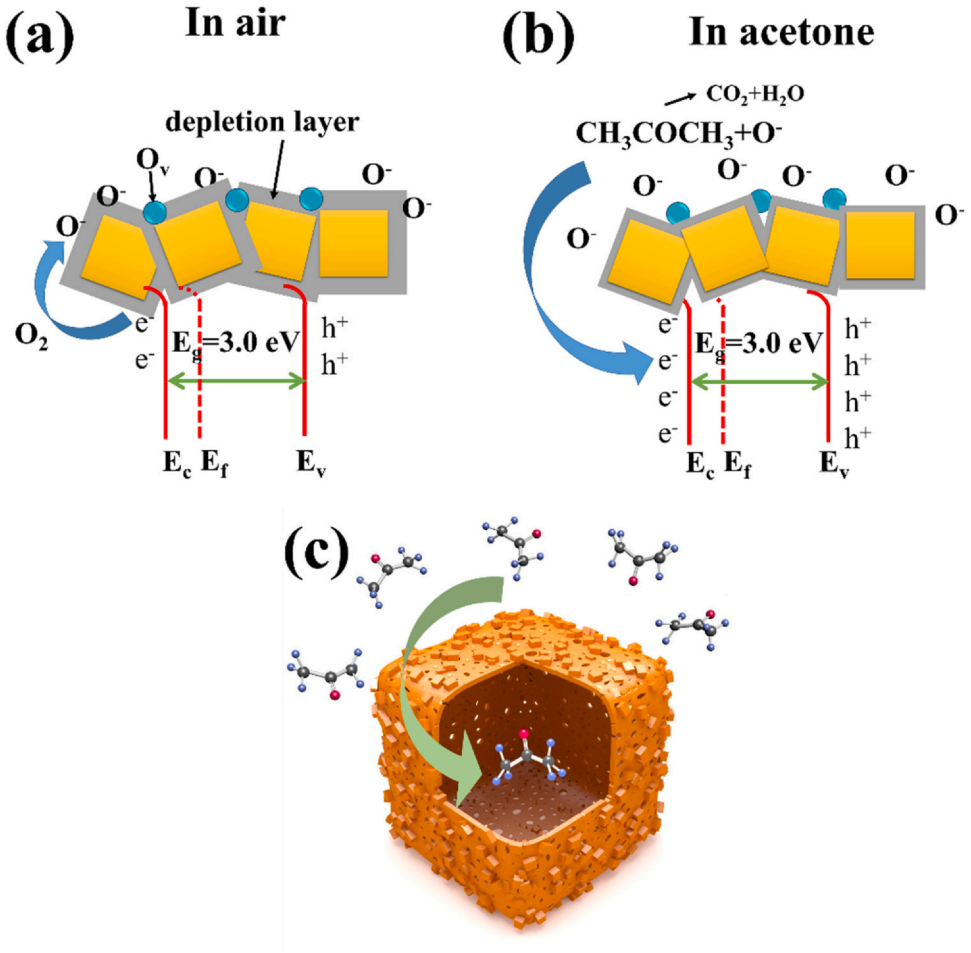

Fig. 6. (a-c) Schematic of the sensing mechanism of N-C@SnO_2-Co_3O_4 HNBs (2.0%).

with the SnO_2-Co_3O_4 HNB derived directly from thermal-decomposition of $CoSn(OH)_6$ precursor, the aim of tailoring the nitrogen-carbon (N-C) dopant did can be achieved by such strategy. The defect characterizations had confirmed the successful preparation of such N-C@SnO_2-Co_3O_4 HNB compound, as well as the generation of oxygen vacancies. Thanks to the N-C dopant as active units for gas sensors, the oxygen vacancies of N-C@SnO_2-Co_3O_4 HNBs (2.0%) were significantly improved which exhibited superior acetone selectivity, lower temperature (160 °C) and excellent response (R_g/R_a = 9.29–50 ppm). This study provided a new perspective for the design of sensing materials *via* rational oxygen vacancy defect engineering, which may offer guidance for the design of other high-performance materials.

Associated content

Supporting information

The Supporting Information is available free of charge on the Journal of Alloys and Compounds publication website: Experimental details; Materials characterization; Gas sensing properties; Illustration of the process of synthesizing N-C@SnO_2-Co_3O_4 HNBs and SnO_2-Co_3O_4 HNBs (Fig. S1); (a-f) Elemental mapping of Sn, Co, O, N and C elements in N-C@SnO_2-Co_3O_4 HNBs (2.0%), and (g) EDS spectrum image (Fig. S2); N_2 adsorption-desorption isotherm and pore size distribution of N-C@SnO_2-Co_3O_4 HNBs (2.0%) (Fig. S3); (a) The TG curves of SnO_2-Co_3O_4 HNBs, and various N-C@SnO_2-Co_3O_4 HNBs (0.9%, 2.0% and 2.5%) products, (b) and (c) The TG-FTIR combining analysis of N-C@SnO_2-Co_3O_4 HNBs (2.0%) with the heating temperature from 30 to 750 °C under N_2 gas, and with the wavenumber of 600–4000 cm^{-1} (Fig. S4); High magnification XPS spectra of (a) C 1 s, (b) N 1 s in N-C@SnO_2-Co_3O_4 HNBs (2.0%), as well as (c) Co 2p, (d) Sn 3d on SnO_2-Co_3O_4 HNBs and N-C@SnO_2-Co_3O_4 HNBs (2.0%), respectively (Fig. S5); SEM images of (a) SnO_2-Co_3O_4 HNBs, (b) N-C@SnO_2-Co_3O_4 HNBs (0.9%), (c) N-C@SnO_2-Co_3O_4 HNBs (2.0%) and (d) N-C@SnO_2-Co_3O_4 HNBs (2.5%) (Fig. S6); PL spectra of SnO_2-Co_3O_4 HNBs and various N-C@SnO_2-Co_3O_4 HNBs (0.9%, 2.0% and 2.5%) products (Fig. S7); Response of SnO_2-Co_3O_4 HNBs and various N-C@SnO_2-Co_3O_4 HNBs (0.9%, 2.0% and 2.5%) sensors to 50 ppm acetone at different working temperatures from 140 to 180 °C in dry air (Fig. S8); (a) Dynamic responses of SnO_2-Co_3O_4 HNBs and various N-C@SnO_2-Co_3O_4 HNBs (0.9%, 2.0% and 2.5%) sensors at 160 °C in the acetone concentration range of 1–50 ppm in dry air, (b) Cyclic sensing response of the four sensors to 50 ppm acetone in dry air, (c) Cyclic sensing response of N-C@SnO_2-Co_3O_4 HNBs (2.0%) to 1 ppm acetone at 160 °C in dry air (Fig. S9); Resistance change of N-C@SnO_2-Co_3O_4 HNBs (2.0%) to 50 ppm acetone with pre-injected various R.Hs. at 160 °C (Fig. S10); Response and recovery of N-C@SnO_2-Co_3O_4 HNBs (2.0%) to 50 ppm acetone in (a) dry air and (b) 90% R.H. at 160 °C (Fig. S11); (a) Dynamic response to different acetone concentrations and (b) cyclic sensing response to 50 ppm acetone of N-C@SnO_2-Co_3O_4 HNBs (2.0%) under 90% R.H. (Fig. S12); Photograph of details for the portable acetone sensing prototype based on the N-C@SnO_2-Co_3O_4 HNBs (2.0%) probe, (c-e) simulated acetone gas testing and transient dynamic response-recovery curves of the sensing prototype to the simulated acetone atmosphere. Insert of (e) is the long term stability tests of the N-C@SnO_2-Co_3O_4 HNBs (2.0%) sensor to 20 ppm acetone at 160 °C (Fig. S13); FTIR spectrum for N-

C@SnO_2-Co_3O_4 HNBs (2.0%) before and after exposure to 50 ppm acetone. The extra appeared peak within the wavenumber of 1000–2000 cm^{-1} indicates the preferred adsorption of acetone on the N-C dopant after N-C@SnO_2-Co_3O_4 HNBs (2.0%) are exposed to acetone (Fig. S14).

CRediT authorship contribution Statement

Ms M. X. Huang initiated the experiments and draft, Mr S. P. Wang, Mr. H. Fu and Ms H. Y. Shao prepared all the samples. Prof. Y. H. Wang and Prof. K. F. Yu offered useful comments on the technical methods. A/Prof. L. W. Wang provided guidance in the research.

Declaration of Competing Interest

The authors declare that they have no known competing financial interests or personal relationships that could have appeared to influence the work reported in this paper.

Acknowledgements

This work is supported by the National Natural Science Foundation of China (Nos. 42030502, 42090041 and 51762005), the Natural Science Foundation of Guangxi Province, China (2017GXNSFAA198254), Science and Technology Project of Guangxi (AD17129063), Science and Technology Major Project of Guangxi (AA17202020, AA17204100, AA18242007).

Appendix A. Supporting information

Supplementary data associated with this article can be found in the online version at doi:10.1016/j.jallcom.2020.158341.

References

[1] H.R. Kim, A. Haensch, I.D. Kim, N. Barsan, U. Weimar, J.H. Lee, The role of NiO doping in reducing the impact of humidity on the performance of SnO_2-based gas sensors: synthesis strategies, and phenomenological and spectroscopic studies, Adv. Funct. Mater. 21 (2011) 4456–4463, https://doi.org/10.1002/adfm.201101154

[2] R. Kumar, N. Goel, M. Kumar, UV-activated MoS_2 based fast and reversible NO_2 sensor at room temperature, ACS Sens. 2 (2017) 1744–1752, https://doi.org/10.1021/acssensors.7b00731

[3] D. Zappa, A. Bertuna, E. Comini, N. Kaur, N. Poli, V. Sberveglieri, G. Sberveglieri, Metal oxide nanostructures: Preparation, characterization and functional applications as chemical sensors, Beilstein J. Nanotechnol. 8 (2017) 1205–1217, https://doi.org/10.3762/bjnano.8.122

[4] E. Maciak, Z. Opilski, M. Urbanczyk, Optical hydrogen sensitivity of Pd-metal oxide composite films prepared on fiber optics, Opt. Fibers Appl. 5952 (2005) 59521R, https://doi.org/10.1117/12.626021

[5] J. Liu, M. Dai, T. Wang, P. Sun, X. Liang, G. Lu, K. Shimanoe, N. Yamazoe, Enhanced gas sensing properties of SnO_2 hollow spheres decorated with CeO_2 nanoparticles heterostructure composite materials, ACS Appl. Mater. Interfaces 8 (2016) 6669–6677, https://doi.org/10.1021/acsami.6b00169

[6] M. Al-Hashem, S. Akbar, P. Morris, Role of oxygen vacancies in nanostructured metal-oxide gas sensors: a review, Sens. Actuators B Chem. 301 (2019) 126845, https://doi.org/10.1016/j.snb.2019.126845

[7] P. Yang, X. Xiao, Y. Li, Y. Ding, P. Qiang, X. Tan, W. Mai, Z. Lin, W. Wu, T. Li, H. Jin, P. Liu, J. Zhou, C.P. Wong, Z.L. Wang, Hydrogenated ZnO core-shell nanocables for flexible supercapacitors and self-powered systems, ACS Nano 7 (2013) 2617–2626, https://doi.org/10.1021/nn306044d

[8] G. Ou, Y. Xu, B. Wen, R. Lin, B. Ge, Y. Tang, Y. Liang, C. Yang, K. Huang, D. Zu, R. Yu, W. Chen, J. Li, H. Wu, L.M. Liu, Y. Li, Tuning defects in oxides at room temperature by lithium reduction, Nat. Commun. 9 (2018) 1–9, https://doi.org/10.1038/s41467-018-03765-0

[9] I.S. Cho, M. Logar, C.H. Lee, L. Cai, F.B. Prinz, X. Zheng, Rapid and controllable flame reduction of TiO_2 nanowires for enhanced solar water-splitting, Nano Lett. 14 (2014) 24–31, https://doi.org/10.1021/nl4026902

[10] Y. Zhong, W. Li, X. Zhao, X. Jiang, S. Lin, Z. Zhen, W. Chen, D. Xie, H. Zhu, High-response room-temperature NO_2 sensor and ultrafast humidity sensor based on SnO_2 with rich oxygen vacancy, ACS Appl. Mater. Interfaces 11 (2019) 13441–13449, https://doi.org/10.1021/acsami.9b01737

[11] A.K. Elger, J. Baranyai, K. Hofmann, C. Hess, Direct operando spectroscopic observation of oxygen vacancies in working Ceria-based gas sensors, ACS Sens. 4 (2019) 1497–1501, https://doi.org/10.1021/acssensors.9b00521

[12] M.-S. Yao, J.-W. Xiu, Q.-Q. Huang, W.-H. Li, W.-W. Wu, A.-Q. Wu, L.-A. Cao, W.-H. Deng, G.-E. Wang, G. Xu, Inside back cover: Van der waals heterostructured MOF-on-MOF thin films: Cascading functionality to realize advanced chemiresistive sensing, Angew. Chem. Int. Ed. 58 (2019) 15161, https://doi.org/10.1002/anie.201910733

[13] M.S. Yao, L.A. Cao, G.L. Hou, M.L. Cai, J.W. Xiu, C.H. Fang, F.L. Yuan, Y.F. Chen, Gold-tin co-sensitized ZnO layered porous nanocrystals: enhanced responses and anti-humidity, RSC Adv. 7 (2017) 20273–20280, https://doi.org/10.1039/c7ra02282d

[14] B. Li, J. Liu, Q. Liu, R. Chen, H. Zhang, J. Yu, D. Song, J. Li, M. Zhang, J. Wang, Core-shell structure of ZnO/Co_3O_4 composites derived from bimetallic-organic frameworks with superior sensing performance for ethanol gas, Appl. Surf. Sci. 475 (2019) 700–709, https://doi.org/10.1016/j.apsusc.2018.12.284

[15] S. Zhang, M. Yang, K. Liang, A. Turak, B. Zhang, D. Meng, C. Wang, F. Qu, W. Cheng, M. Yang, An acetone gas sensor based on nanosized Pt-loaded Fe_2O_3 nanocubes, Sens. Actuators B Chem. 290 (2019) 59–67, https://doi.org/10.1016/j.snb.2019.03.082

[16] H. Fu, H. Shao, L. Wang, H. Jin, D. Xia, S. Deng, Y. Wang, Y. Chen, C. Hua, L. Liu, L. Zang, From a relatively hydrophobic and triethylamine (TEA) adsorption-selective core-shell heterostructure to a humidity-resistant and TEA highly selective sensing prototype: an alternative approach to improve the sensing characteristics of TEA sensors, ACS Sens. 5 (2020) 571–579, https://doi.org/10.1021/acssensors.9b02519

[17] H. Shao, M. Huang, H. Fu, S. Wang, L. Wang, J. Lu, Y. Wang, K. Yu, Hollow WO_3/SnO_2 hetero-nanofibers: controlled synthesis and high efficiency of acetone vapor detection, Front. Chem. 7 (2019) 1–10, https://doi.org/10.3389/fchem.2019.00785

[18] M. Weber, J.H. Kim, J.H. Lee, J.Y. Kim, I. Iatsunskyi, E. Coy, M. Drobek, A. Julbe, M. Bechelany, S.S. Kim, High-performance nanowire hydrogen sensors by exploiting the synergistic effect of Pd nanoparticles and metal-organic framework membranes, ACS Appl. Mater. Interfaces 10 (2018) 34765–34773, https://doi.org/10.1021/acsami.8b12569

[19] Q. Jia, H. Ji, Y. Zhang, Y. Chen, X. Sun, Z. Jin, Rapid and selective detection of acetone using hierarchical ZnO gas sensor for hazardous odor markers application, J. Hazard. Mater. 276 (2014) 262–270, https://doi.org/10.1016/j.jhazmat.2014.05.044

[20] R.L. Wilson, C.E. Simion, A. Stanoiu, A. Taylor, S. Guldin, J.A. Covington, C.J. Carmalt, C.S. Blackman, Humidity-tolerant ultrathin NiO gas-sensing films, ACS Sens. 5 (2020) 1389–1397, https://doi.org/10.1021/acssensors.0c00172

[21] C. Su, L. Zhang, Y. Han, X. Chen, S. Wang, M. Zeng, N. Hu, Y. Su, Z. Zhou, H. Wei, Z. Yang, Glucose-assisted synthesis of hierarchical flower-like Co_3O_4 nanostructures assembled by porous nanosheets for enhanced acetone sensing, Sens. Actuators B Chem. 288 (2019) 699–706, https://doi.org/10.1016/j.snb.2019.03.004

[22] T. Zhou, X. Liu, R. Zhang, Y. Wang, T. Zhang, NiO/$NiCo_2O_4$ truncated nanocages with PdO catalyst functionalization as sensing layers for acetone detection, ACS Appl. Mater. Interfaces 10 (2018) 37242–37250, https://doi.org/10.1021/acsami.8b12981

[23] Z. Sun, J. Lin, K. Hou, L. Guan, H. Zhan, Pore engineering of an Fe-N-C electrocatalyst to enhance the performance for the oxygen reduction reaction by adding g-C_3N_4 into polyaniline and cyanamide as a precursor, J. Mater. Chem. A 8 (2020) 7273–7279, https://doi.org/10.1039/c9ta13831e

[24] W. Liu, Y. Xie, T. Chen, Q. Lu, S. Ur Rehman, L. Zhu, Rationally designed mesoporous In_2O_3 nanofibers functionalized Pt catalysts for high-performance acetone gas sensors, Sens. Actuators B Chem. 298 (2019) 126871, https://doi.org/10.1016/j.snb.2019.126871

[25] J. Guo, Z. Yang, Y. Yu, H.D. Abruña, L.A. Archer, Lithium-sulfur battery cathode enabled by lithium-nitrile interaction, J. Am. Chem. Soc. 135 (2013) 763–767, https://doi.org/10.1021/ja309435f

[26] Z. Wang, Y. Dong, H. Li, Z. Zhao, H. Bin Wu, C. Hao, S. Liu, J. Qiu, X.W.D. Lou, Enhancing lithium-sulphur battery performance by strongly binding the discharge products on amino-functionalized reduced graphene oxide, Nat. Commun. 5 (2014) 1–8, https://doi.org/10.1038/ncomms6002

[27] R. Chen, T. Zhao, J. Lu, F. Wu, L. Li, J. Chen, G. Tan, Graphene-based three-dimensional hierarchical sandwich-type architecture for high-performance Li/S batteries, 2013.

[28] M.X. Pulikkathara, O.V. Kuznetsov, V.N. Khabashesku, Sidewall covalent functionalization of single wall carbon nanotubes through reactions of fluoronanotubes with urea, guanidine, and thiourea, Chem. Mater. 20 (2008) 2685–2695, https://doi.org/10.1021/cm7035037

[29] G.C. Li, G.R. Li, S.H. Ye, X.P. Gao, A Polyaniline-coated sulfur/carbon composite with an enhanced high-rate capability as a cathode material for lithium/sulfur batteries, Adv. Energy Mater. 2 (2012) 1238–1245, https://doi.org/10.1002/aenm.201200017

[30] L. Zhang, J. Ran, S.-Z. Qiao, M. Jaroniec, Characterization of semiconductor photocatalysts, Chem. Soc. Rev. 48 (2019) 5184–5206, https://doi.org/10.1039/c9cs00172g

[31] Y. Lü, W. Zhan, Y. He, Y. Wang, X. Kong, Q. Kuang, Z. Xie, L. Zheng, MOF-templated synthesis of porous Co_3O_4 concave nanocubes with high specific surface area and their gas sensing properties, ACS Appl. Mater. Interfaces 6 (2014) 4186–4195, https://doi.org/10.1021/am405858v

[32] Y. Tong, P. Chen, T. Zhou, K. Xu, W. Chu, C. Wu, Y. Xie, A bifunctional hybrid electrocatalyst for oxygen reduction and evolution: Cobalt oxide nanoparticles strongly coupled to B, N-decorated graphene, Angew. Chem. Int. Ed. 56 (2017) 7121–7125, https://doi.org/10.1002/anie.201702430

[33] X.B. Li, S.Y. Ma, F.M. Li, Y. Chen, Q.Q. Zhang, X.H. Yang, C.Y. Wang, J. Zhu, Porous spheres-like ZnO nanostructure as sensitive gas sensors for acetone detection, Mater. Lett. 100 (2013) 119–123, https://doi.org/10.1016/j.matlet.2013.02.117

[34] M.A. Peck, M.A. Langell, Comparison of nanoscaled and bulk NiO structural and environmental characteristics by XRD, XAFS, and XPS, Chem. Mater. 24 (2012) 4483–4490, https://doi.org/10.1021/cm300739y
[35] D.C. Koningsberger, B.L. Mojet, G.E. Van Dorssen, D.E. Ramaker, XAFS spectroscopy; fundamental principles and data analysis, Top. Catal. 10 (2000) 143–155, https://doi.org/10.1023/A:1019105310221
[36] S. Nayak, K. Dasari, D.C. Joshi, P. Pramanik, R. Palai, V. Sathe, S. Thota, The spectroscopic studies of Co3O4, 2 2011, pp. 1–12.
[37] L.Z. Liu, T.H. Li, X.L. Wu, J.C. Shen, P.K. Chu, Identification of oxygen vacancy types from Raman spectra of SnO_2 nanocrystals, J. Raman Spectrosc. 43 (2012) 1423–1426, https://doi.org/10.1002/jrs.4078
[38] P.G. Li, M. Lei, W.H. Tang, X. Guo, X. Wang, Facile route to straight SnO_2 nanowires and their optical properties, J. Alloy. Compd. 477 (2009) 515–518, https://doi.org/10.1016/j.jallcom.2008.10.130
[39] W. Fan, H. Li, F. Zhao, X. Xiao, Y. Huang, H. Ji, Y. Tong, Boosting the photocatalytic performance of (001) BiOI: enhancing donor density and separation efficiency of photogenerated electrons and holes, Chem. Commun. 52 (2016) 5316–5319, https://doi.org/10.1039/c6cc00903d
[40] H. Yuan, S.A.A.A. Aljneibi, J. Yuan, Y. Wang, H. Liu, J. Fang, C. Tang, X. Yan, H. Cai, Y. Gu, S.J. Pennycook, J. Tao, D. Zhao, ZnO nanosheets abundant in oxygen vacancies derived from metal-organic frameworks for ppb-level gas sensing, Adv. Mater. 31 (2019) 1–9, https://doi.org/10.1002/adma.201807161
[41] C.H. Drake, S. Seal, Understanding the low temperature electrical properties of nanocrystalline tin oxide for gas sensor applications, Ph.D. 2007, 124. http://search.proquest.com/docview/304745459.
[42] F. Liu, X. Wang, X. Chen, X. Song, J. Tian, H. Cui, Porous ZnO ultrathin nanosheets with high specific surface areas and abundant oxygen vacancies for acetylacetone gas sensing, ACS Appl. Mater. Interfaces 11 (2019) 24757–24763, https://doi.org/10.1021/acsami.9b06701
[43] J.-S. Kim, C.W. Na, C.-H. Kwak, H.-Y. Li, J.W. Yoon, J.-H. Kim, S.-Y. Jeong, J.-H. Lee, Humidity-independent gas sensors using Pr-doped In_2O_3 macroporous spheres: role of cyclic Pr^{3+}/Pr^{4+} redox reactions in suppression of water-poisoning effect, ACS Appl. Mater. Interfaces 11 (2019) 25322–25329, https://doi.org/10.1021/acsami.9b06386
[44] C.H. Kwak, T.H. Kim, S.Y. Jeong, J.W. Yoon, J.S. Kim, J.H. Lee, Humidity-independent oxide semiconductor chemiresistors using terbium-doped SnO_2 yolk-shell spheres for real-time breath analysis, ACS Appl. Mater. Interfaces 10 (2018) 18886–18894, https://doi.org/10.1021/acsami.8b04245
[45] Z. Chen, C. Lu, Humidity sensors: a review of materials and mechanisms, Sens. Lett. 3 (2005) 274–295, https://doi.org/10.1166/sl.2005.045
[46] H. Zhu, Q. Li, Y. Ren, Q. Gao, J. Chen, N. Wang, J. Deng, X. Xing, A new insight into cross-sensitivity to humidity of SnO_2 sensor, Small 14 (2018) 1–6, https://doi.org/10.1002/smll.201703974
[47] N.K. Pandey, K. Tiwari, A. Roy, Characterization and humidity sensing application of ZnO-TiO_2 nanocomposite, Adv. Mater. Res. 304 (2011) 48–52, https://doi.org/10.4028/www.scientific.net/AMR.304.48
[48] N. Yamazoe, J. Fuchigami, M. Kishikawa, T. Seiyama, Interactions of tin oxide surface with O_2, H_2O and H_2, Surf. Sci. 86 (1979) 335–344, https://doi.org/10.1016/0039-6028(79)90411-4
[49] J.F. Boyle, K.A. Jones, The effects of CO, water vapor and surface temperature on the conductivity of a SnO_2 gas sensor, J. Electron. Mater. 6 (1977) 717–733, https://doi.org/10.1007/BF02660346
[50] Y. Shimizu, Humidity-sensitive characteristics of La^{3+}-doped and undoped $SrSnO_3$, J. Electrochem. Soc. 136 (1989) 1206–1210, https://doi.org/10.1149/1.2096854
[51] M. Gong, Y. Li, Y. Guo, X. Lv, X. Dou, 2D TiO_2 nanosheets for ultrasensitive humidity sensing application benefited by abundant surface oxygen vacancy defects, Sens. Actuators B Chem. 262 (2018) 350–358, https://doi.org/10.1016/j.snb.2018.01.187
[52] B. Zhang, M. Cheng, G. Liu, Y. Gao, L. Zhao, S. Li, Y. Wang, F. Liu, X. Liang, T. Zhang, G. Lu, Room temperature NO_2 gas sensor based on porous Co_3O_4 slices/reduced graphene oxide hybrid, Elsevier B.V., 2018, https://doi.org/10.1016/j.snb.2018.02.117
[53] L. Wang, H. Fu, Q. Jin, H. Jin, H. Haick, S. Wang, K. Yu, S. Deng, Y. Wang, Directly transforming SnS_2 nanosheets to hierarchical SnO_2 nanotubes: towards sensitive and selective sensing of acetone at relatively low operating temperatures, Sens. Actuators B Chem. 292 (2019) 148–155, https://doi.org/10.1016/j.snb.2019.04.127
[54] X. Kou, C. Wang, M. Ding, C. Feng, X. Li, J. Ma, H. Zhang, Y. Sun, G. Lu, Synthesis of Co-doped SnO2 nanofibers and their enhanced gas-sensing properties, Sens. Actuators B Chem. 236 (2016) 425–432, https://doi.org/10.1016/j.snb.2016.06.006
[55] A. Koo, R. Yoo, S.P. Woo, H.S. Lee, W. Lee, Enhanced acetone-sensing properties of Pt-decorated Al-doped ZnO nanoparticles, Sens. Actuators, B Chem. 280 (2019) 109–119, https://doi.org/10.1016/j.snb.2018.10.049
[56] H. Fu, H. Shao, L. Wang, H. Jin, D. Xia, S. Deng, Y. Wang, Y. Chen, C. Hua, L. Liu, L. Zang, From a relatively Hydrophobic and Triethylamine (TEA) adsorption-selective core-shell heterostructure to a humidity-resistant and TEA highly selective sensing prototype: an alternative approach to improve the sensing characteristics of TEA sensors, ACS Sens. 5 (2020) 571–579, https://doi.org/10.1021/acssensors.9b02519
[57] C. Zhai, M. Zhu, L. Jiang, T. Yang, Q. Zhao, Y. Luo, M. Zhang, Fast triethylamine gas sensing response properties of nanosheets assembled WO_3 hollow microspheres, Appl. Surf. Sci. 463 (2019) 1078–1084, https://doi.org/10.1016/j.apsusc.2018.09.049
[58] M. Sasaki, K. Suematsu, M. Yuasa, T. Kida, K. Shimanoe, Effect of water vapor on Pd-loaded SnO_2 nanoparticles gas sensor, ACS Appl. Mater. Interfaces 7 (2015) 5863–5869, https://doi.org/10.1021/am509082w
[59] W. Yang, L. Feng, S. He, L. Liu, S. Liu, Density gradient strategy for preparation of broken In_2O_3 microtubes with remarkably selective detection of triethylamine vapor, ACS Appl. Mater. Interfaces 10 (2018) 27131–27140, https://doi.org/10.1021/acsami.8b09375